Future Cities and Environment
ISSN 2363-9075 Volume 12 (2026)

https://doi.org/10.70917/fce-2026-020

Article

Ultimate Capacity of Subsea CO_2 Transport Pipelines with Semi-Elliptical Corrosion Defects under Combined Internal Pressure and Bending Moment: A Finite Element Study

Aprianur Fajri [1,2,3], Aditya Rio Prabowo [1,2,*], Ristiyanto Adiputra [4], Nurul Muhayat [1], Iwan Istanto [1], Dominicus Danardono Dwi Prija Tjahjana [1], Quang Thang Do [5], Nguyen Thanh Phuong [6], and Oleksiy Melnyk [7]

1 Department of Mechanical Engineering, Universitas Sebelas Maret, Surakarta 57126, Indonesia; (A.F; https://orcid.org/0009-0000-1759-2397); (A.R.P; https://orcid.org/0000-0001-5217-5943); (N.M; https://orcid.org/0000-0002-1086-7826); (I.I; https://orcid.org/0009-0009-9037-4375); (D.D.D.P.T; https://orcid.org/0009-0005-2278-5405).
2 Laboratory of Designs and Computational Mechanics, Faculty of Engineering, Universitas Sebelas Maret, Surakarta 57126, Indonesia.
3 Department of Manufacturing Engineering Technology, Akademi Inovasi Indonesia, Salatiga 50721, Indonesia.
4 Research Center for Hydrodynamics Technology, National Research and Innovation Agency (BRIN), Surabaya 60117, Indonesia; (R.A; https://orcid.org/0000-0003-3630-9432).
5 Department of Naval Architecture and Ocean Engineering, Nha Trang University, Nha Trang 650000, Vietnam; (Q.T.D; https://orcid.org/0000-0002-4232-9563).
6 Department of Electronic – Electrical Engineering, Nha Trang University, Nha Trang 650000, Vietnam; (N.T.P; https://orcid.org/0000-0002-7220-7356).
7 Department of Navigation and Maritime Safety, Odesa National Maritime University, Odesa 65029, Ukraine; (O.M; https://orcid.org/0000-0001-9228-8459).
* Correspondence author: aditya@ft.uns.ac.id

Abstract: This study investigates the ultimate bending capacity of API 5L X52 subsea CO_2 transport pipelines as part of environmentally sound technology within Sustainable Development Goal (SDG) 17, incorporating idealized semi-elliptical corrosion defects under combined internal pressure and bending moment. A nonlinear finite element model was benchmarked against published four-point bending tests on corroded pipes with rectangular defects for validation purposes. The validated modeling procedure was then applied to a deterministic parametric study involving 33 selected cases, with corrosion depth ratios of d/t= 0.1 – 0.8, defect length ratios of l/D= 0.2 – 1.2, and internal pressures ranging from 0 to 20 MPa. The results show that corrosion depth is the primary parameter controlling bending-capacity degradation because it reduces the residual wall thickness, local section stiffness, and shell stability at the remaining ligament. Increasing defect length reduces the bending capacity up to a saturation region, after which the response is mainly governed by the weakest local cross-section. For the investigated semi-elliptical defect configuration, internal pressure reduces the ultimate bending capacity rather than improving it. The pressure-induced circumferential stress interacts with the bending-induced axial stress, promoting earlier yielding and local buckling at the corroded ligament. The normalized ultimate bending capacity at $d/t = 0.5$ and $l/D = 1.0$ decreased from 0.95 to 0.86 as the pressure increased from 0 to 20 MPa. These findings indicate that the residual bending capacity of corroded CO_2 pipelines should be assessed by considering the coupled effects of metal-loss geometry, pressure-induced membrane stress, and local shell instability. The results are deterministic estimates and are limited to the investigated pipe geometry, idealized single-defect morphology, material model, and loading range. The benchmark validation supports the FE framework but does not directly validate the semi-elliptical defect morphology.

Keywords: CO_2 transport; environmentally sound technology; subsea pipeline; corrosion defect; finite element analysis; ultimate capacity

Nomenclature

Latin Symbols

d	corrosion depth (mm)
D	outer diameter of pipe (mm)
D_m	mean diameter of pipe (mm)
D_s	local shell bending rigidity (Nmm)
E	elastic modulus (GPa)
I	second moment of area (mm^4)
l	corrosion length (mm)
L	pipe length (mm)
M	bending moment obtained from the FE response at a given rotation (kNm)
M_{ref}	reference bending moment used for normalization (kNm)
M_u	ultimate bending moment obtained from FE simulation (kNm)
$\bar{M}$	normalized bending moment
$\overline{M_u}$	normalized ultimate bending moment
n	number of elements through pipe wall thickness
P	internal pressure applied (MPa)
P_{ref}	reference internal pressure (MPa)
$\bar{P}$	normalized internal pressure
R	pipe radius (mm)
t	nominal pipe wall thickness (mm)
t_d	residual wall thickness at corrosion defect (mm)
w	corrosion width (mm)
y	distance from neutral axis (mm)
Z	elastic section modulus (mm^3)
Z_d	local section modulus at defect region (mm^3)
Z_p	plastic section modulus (mm^3)

Greek Symbols

κ	curvature (mm^{-1})
ν	Poisson's ratio
θ	rotational displacement or pipe-end rotation (rad)
σ_b	longitudinal bending stress at a distance y from the neutral axis (MPa)
$\sigma_{b,max}$	extreme-fiber longitudinal bending stress of the intact section (MPa)
$\sigma_{b,d}$	local longitudinal bending stress at the corroded ligament (MPa)
$\sigma_{cr,d}$	local critical compressive shell-buckling stress at the defect region (MPa)
σ_h	hoop membrane stress induced by internal pressure in the nominal wall (MPa)
$\sigma_{h,d}$	local hoop membrane stress induced by internal pressure at the defect region (MPa)
σ_l	longitudinal membrane stress induced by internal pressure in the nominal wall (MPa)
$\sigma_{l,d}$	local longitudinal membrane stress induced by internal pressure at the defect region (MPa)
σ_{ref}	reference stress (MPa)
σ_U	ultimate tensile strength of material (MPa)
σ_y	yield strength of material (MPa)
σ_{vm}	von Mises equivalent stress (MPa)
$\sigma_{vm,d}$	local von Mises equivalent stress at the defect region (MPa)
$\sigma_{z,d}$	total local longitudinal stress at the defect region (MPa)
$\sigma_{\theta,d}$	total circumferential stress at the defect used in the equivalent-stress interaction (MPa)
$\tau_{\theta z}$	in-plane shear stress component (MPa)

1. Introduction

The safe transportation of captured carbon dioxide (CO_2) to offshore geological storage sites is a critical component of carbon capture and storage (CCS) systems, which are among the instruments of environmentally sound technologies (Sustainable Development Goals - SDGs 17). In offshore applications, CO_2 is transported through subsea pipelines that operate under high internal pressure. These pipelines are also subjected to environmental and geotechnical actions, such as seabed movement, sediment transport, free spanning, differential settlement, and lateral instability. Under such conditions, the structural integrity of the pipeline is governed not only by pressure-induced membrane stresses but also by bending-induced compressive strain and local instability.

During long-term service, subsea pipelines are exposed to aggressive marine environments. Prolonged exposure to seawater, biofouling, deposit accumulation, coating degradation, and inadequate cathodic protection can promote localized corrosion. Biofouling and deposits may further intensify corrosion. Localized corrosion produces metal-loss defects, which reduce the effective wall thickness and create local stress concentrations. These defects can significantly degrade the residual load-carrying capacity of the pipe (Udonsek, Tamonodukobipi and Odokwo, 2023; Riffat, Doudran, and Samaei, 2025; Riffat, Nazari and Samaei, 2026; Zhou *et al.*, 2026). When corrosion damage occurs in a pipe under bending, plastic strain localization may develop near the defect and eventually trigger local buckling or plastic collapse. Therefore, evaluating the ultimate strength of corroded pipelines under realistic combined loading conditions is essential for integrity assessment, life-extension decisions, and safe operation of subsea CO_2 transport systems (Bhardwaj, Teixeira and Soares, 2020; Chen *et al.*, 2024).

Extensive research has been conducted on the structural strength of pipelines under different loading conditions. Early studies mainly investigated intact pipes subjected to single loading components, such as internal pressure, bending moment, axial force, or external pressure. These studies established fundamental collapse mechanisms, including burst failure governed by membrane stress and local buckling governed by cross-sectional ovalization. Subsequent investigations focused on pipelines with corrosion defects, particularly regarding burst pressure prediction under internal pressure. In many of these studies, corrosion defects were idealized as rectangular metal-loss regions in accordance with simplified engineering assessment procedures (Lo, Karuppanan and Ovinis, 2022). More recent numerical and experimental studies have introduced more realistic defect morphologies, including elliptical, semi-elliptical, and pitting-type corrosion defects, to better represent localized metal loss observed in service (Shuai *et al.*, 2022; Zhou *et al.*, 2025).

Other researchers have examined the bending resistance of corroded pipelines. These studies showed that corrosion reduces flexural capacity primarily through section loss and strain concentration at the defect location. However, most investigations considered pure bending conditions without internal pressure. More recent work has addressed combined loading conditions in pipelines, such as bending with axial force or external pressure. These studies demonstrated complex interactions between membrane stress and bending deformation (Gao *et al.*, 2024; Ma *et al.*, 2025; Zhang *et al.*, 2025). However, the available literature provides limited evidence on corroded pipelines subjected simultaneously to bending moment and internal pressure. Most studies focus on burst failure or use rectangular and other idealized defect profiles. Gradual wall-thinning geometries, such as semi-elliptical metal loss, remain underexamined under bending-dominated loading. Consequently, the interaction between semi-elliptical wall thinning, pressure-induced membrane stress, and bending-induced local instability remains insufficiently quantified.

Accordingly, this study evaluates the ultimate bending capacity of API 5L X52 pipe models containing idealized semi-elliptical corrosion defects under combined internal pressure and bending moment. It does not aim to propose a new finite element formulation or a closed-form failure criterion. Instead, it examines how gradual wall thinning affects stress concentration, plastic localization, and local buckling during bending-dominated collapse. The specific objectives are: (i) to evaluate the normalized ultimate bending capacity of pipes containing semi-elliptical corrosion defects, (ii) to examine the effect of internal pressure on bending collapse at the corroded ligament, and (iii) to quantify the influence of corrosion depth, defect axial length, and pressure level on residual bending resistance within the investigated parameter range.

2. Ultimate Bending Capacity and Combined Pressure–Bending Framework

The FE results are presented in normalized form to enable consistent comparison across defect geometries and pressure levels. The reference bending moment and pressure are nominal scaling quantities derived from the intact-pipe geometry and material properties. They are used to organize the FE results and do not constitute independent collapse criteria or design resistance values.

2.1. Reference Bending Moment for Normalization

For a circular pipe subjected to bending, the bending resistance can be related to the formation of a plastic stress distribution over the cross-section. In the present study, a reference bending moment is defined using the plastic section modulus and a reference stress for normalization of the FE-derived bending response, as expressed in Eq. (1):

$$M_{ref} = \sigma_{ref} Z_p \tag{1}$$

The plastic section modulus of the hollow circular section is calculated as:

$$Z_p = \frac{D^3-(D-2t)^3}{6} \tag{2}$$

where D is outer diameter and t is the nominal wall thickness. This expression is obtained from the plastic bending formulation of circular sections by subtracting the contribution of inner void from the outer cross-section (Korol and Hudoba, 1972; Elchalakani, Zhao and Grzebieta, 2002; Conde *et al.*, 2023). Because the present analysis involves large plastic deformation prior to collapse, a reference stress is adopted instead of using only the yield strength or ultimate tensile strength. The reference stress is defined as:

$$\sigma_{ref} = \frac{\sigma_y+\sigma_U}{2} \tag{3}$$

where σ_y is the yield strength and σ_U is the ultimate tensile strength of the pipe material. The reference stress in Eq. (3) is used solely to define the nominal scaling moment (M_{ref}). In this calculation, (σ_U) denotes the engineering ultimate tensile strength of 520 MPa, whereas the true stress–plastic strain curve is used only for the nonlinear material definition in the FE model.

2.2. FE-Derived Ultimate Bending Moment and Normalization

In the finite element simulations, the bending response is obtained as a moment–rotation curve. Since the loading is imposed through rotational or displacement-controlled deformation, the bending moment (M) is obtained from the FE reaction response at each rotation level. The ultimate bending moment (M_u) is defined as the peak bending moment obtained from this curve. This value represents the maximum FE-derived bending resistance reached by the pipe before significant post-peak softening or localized instability develops. The bending moment and ultimate bending moment are normalized by the theoretical reference bending capacity as follows:

$$\bar{M} = \frac{M}{M_{ref}};\ \bar{M}_u = \frac{M_u}{M_{ref}}; \tag{4}$$

The normalized bending moment ($\bar{M}$) describes the instantaneous FE response, while $\bar{M}_u$ denotes the peak FE-derived bending moment expressed relative to the same nominal reference moment. These quantities are used to compare the effects of corrosion geometry and internal pressure across the investigated cases.

2.3. Reference Internal Pressure

The applied internal pressure is normalized using a reference pressure derived from the thin-walled hoop-stress relation for a defect-free pipe:

$$P_{ref} = \frac{2\sigma_{ref}t}{D} \tag{5}$$

The normalized internal pressure is then defined as:

$$\bar{P} = \frac{P}{P_{ref}} \tag{6}$$

where P is the applied internal pressure. In Eq. (5), the outer diameter is used as the nominal diameter for normalization. This definition allows the pressure level to be expressed relative to the intact pipe's pressure-carrying capacity. In the present study, internal pressure is not treated only as a burst-loading component. Instead, it is considered as a membrane-stress component that interacts with bending-induced stress and local instability at the corrosion defect. This interpretation is consistent with thin-walled pressure vessel theory and burst-pressure formulations for line pipes (Zhu and Leis, 2012; Sinclair and Helms, 2015).

2.4. Bending Stress and Section Loss at the Corrosion Defect

Under bending, the longitudinal stress in an ideal elastic pipe section is expressed as:

$$\sigma_b = \frac{My}{I} \tag{7}$$

where M is the bending moment corresponding to the considered rotation level, y is the distance from the neutral axis, and I is the second moment of area. At the extreme fiber of the cross-section, Eq. (7) can be written as:

$$\sigma_{b,max} = \frac{M}{Z} \tag{8}$$

where Z is the elastic section modulus of the intact pipe.

For a corroded pipe, the local residual wall thickness at the defect region is:

$$t_d = t - d \tag{9}$$

where d is the corrosion depth. The reduction in wall thickness decreases the local section modulus at the defect region. Therefore, the local bending stress at the corroded ligament may be approximated as:

$$\sigma_{b,d} \approx \frac{M}{Z_d} \tag{10}$$

where $Z_d < Z$. Eq. (10) indicates that, for the same bending moment response, the local bending stress in the corroded region becomes higher than that in the intact section because the local section modulus is reduced. For interpretive purposes, the ultimate bending resistance of a corroded pipe may be related to the local section modulus of the weakened defect region:

$$M_u \propto \sigma_y Z_d \tag{11}$$

For a first-order thin-walled approximation, the reduction in local section modulus may be related to the remaining wall thickness as:

$$\frac{Z_d}{Z} \approx \frac{t_d}{t} = 1 - \frac{d}{t} \tag{12}$$

Eq. (12) is not used as a closed-form design equation in this study. Instead, it provides a mechanical interpretation of why the depth of corrosion strongly affects the ultimate bending capacity. In the nonlinear regime, the actual capacity reduction is also influenced by stress concentration, plastic strain localization, pressure-induced membrane stress, ovalization, and local shell buckling.

2.5. Pressure-Induced Membrane Stresses

For a thin-walled pipe subjected to internal pressure, the hoop and longitudinal membrane stresses can be approximated as:

$$\sigma_h = \frac{PD_m}{2t} \tag{13}$$

$$\sigma_l = \frac{PD_m}{4t} \tag{14}$$

where D_m is the mean diameter of the pipe. The longitudinal pressure stress in Eq. (14) is interpreted as the membrane stress component associated with a closed-ended or axially restrained pressurized pipe condition. In the corroded region, the effective wall thickness is reduced from t to t_d. Therefore, the local hoop and longitudinal membrane stresses increase approximately as:

$$\sigma_{h,d} \approx \frac{PD_m}{2t_d} \tag{15}$$

$$\sigma_{l,d} \approx \frac{PD_m}{4t_d} \tag{16}$$

Eqs. (14) and (16) represent the conventional closed-ended or axially restrained pressure-vessel condition, in which internal pressure produces an axial pressure thrust that is transmitted through the pipe wall. These equations are included as reference relations for pressurized pipelines with sealed ends or axial restraint. In the present FE model, pressure was applied only to the pipe's cylindrical inner surface. No end-cap pressure or equivalent axial pressure thrust was imposed. Therefore, Eqs. (14) and (16) were not used to define the FE loading condition. The present numerical response is primarily associated with pressure-induced circumferential stress, bending-induced axial stress, and the local three-dimensional stress state at the corrosion defect.

2.6. Local Shell Instability at Corrosion Defects

In addition to reducing the section modulus, corrosion also reduces the local shell stiffness. The shell bending rigidity at the defect region can be expressed as:

$$D_s = \frac{Et_d^3}{12(1-\upsilon^2)} \quad (17)$$

where E is the elastic modulus and υ is Poisson's ratio. Eq. (17) indicates that shell bending rigidity is highly sensitive to wall thickness because it varies with the third power of t_d.

The local critical compressive stress for a cylindrical shell is commonly related to the thickness-to-radius ratio as:

$$\sigma_{cr,d} \propto \frac{E}{\sqrt{3(1-\upsilon^2)}}\left(\frac{t_d}{R}\right) \quad (18)$$

where R is the pipe radius. Eqs. (17) and (18) indicate that a reduction in residual wall thickness decreases the resistance of the pipe wall to ovalization, wrinkling, and local buckling. Therefore, the collapse of a corroded pipe under bending is governed not only by net-section loss but also by the interaction between plastic yielding and local shell instability.

2.7. Combined Pressure–Bending Stress Interaction

The mechanical response of a corroded pipe under combined internal pressure and bending can be interpreted in terms of the interaction among pressure-induced membrane stress, bending-induced longitudinal stress, and local shell instability at the defect. Although the nonlinear finite element model directly accounts for the three-dimensional stress state, the following relations provide a useful mechanical basis for interpreting the numerical results.

For a general closed-ended or axially restrained pipe, the total local longitudinal stress at the defect region may be approximated as the superposition of pressure-induced longitudinal membrane stress and bending stress:

$$\sigma_{z,d} \approx \sigma_{l,d} \pm \sigma_{b,d} \quad (19)$$

In the FE model, the local axial stress is evaluated directly from the computed stress field; Eq. (19) is included only as a closed-ended reference relation. The sign of the bending stress depends on whether the evaluated point is located on the tensile or compressive side of the pipe wall. Then, the local circumferential stress is mainly governed by the pressure-induced hoop stress:

$$\sigma_{\theta,d} \approx \sigma_{h,d} \quad (20)$$

Accordingly, the local equivalent stress at the defect region can be interpreted using the von Mises stress measure:

$$\sigma_{vm,d} = \left[\sigma_{\theta,d}^2 + \sigma_{z,d}^2 - \sigma_{\theta,d}\sigma_{z,d} + 3\tau_{\theta,z}^2\right]^{\frac{1}{2}} \quad (21)$$

where $\tau_{\theta,z}$ is the in-plane shear stress component. Eq. (21) indicates that internal pressure reduces the remaining stress margin available for additional bending deformation, particularly in the corroded ligament where the wall thickness is reduced. Therefore, internal pressure may accelerate yielding and local instability under bending, even when the applied pressure remains below the intact pipe's reference pressure.

The global bending deformation can be related to curvature through the elastic flexural relation:

$$\kappa = \frac{M}{EI} \quad (22)$$

and the corresponding rotational displacement may be expressed as:

$$\theta = \int \kappa \, dx \quad (23)$$

Eqs. (22) and (23) are used only as interpretive measures for the initial flexural response. At large deformation, the ultimate response is governed by nonlinear material behavior, cross-sectional ovalization, plastic strain localization, and local shell buckling.

3. Materials and Methods

3.1. FE Validation

The four-point bending test on pipes with rectangular corrosion defects (see Fig. 1) reported by Yu, Vargas and Karr (2012) was re-simulated using the finite element method (FEM) under nonlinear static loading conditions. ANSYS Workbench served as the pre- and post-processing environment, while the structural response was computed using the implicit finite element solver ANSYS Mechanical. The bending load was applied in a displacement-controlled manner to maintain solution stability during nonlinear plastic deformation and local buckling.

The pipe used in this validation procedure was made of API 5L X52 steel, with an outer diameter of 219.08 mm, a length of 6096 mm, and a thickness of 12.7 mm. The corrosion defect configuration adopted from the reference test had a depth of $0.5t$ and a circumferential extent of 30°. Two loading conditions were simulated: pure bending and combined bending with an internal pressure of 24.94 MPa. In the experimental setup of Yu, Vargas and Karr (2012), internal pressure was applied by sealing both pipe ends and injecting fluid into the specimen. In the present numerical model, the fluid domain was not explicitly modeled; instead, the internal pressure was applied as a uniformly distributed normal force on the pipe's inner surface. The boundary conditions corresponding to this procedure are illustrated in Fig. 2. The full-scale model was discretized using three-dimensional solid elements, resulting in 37,970 nodes and 19,204 elements. Mesh refinement was introduced in the defect and contact regions to accurately capture local stress concentration and deformation behavior. The mesh quality was controlled by maintaining a Jacobian ratio greater than 0.9 in the critical regions. A mesh convergence study was also conducted to ensure that the numerical results were not strongly dependent on element size.

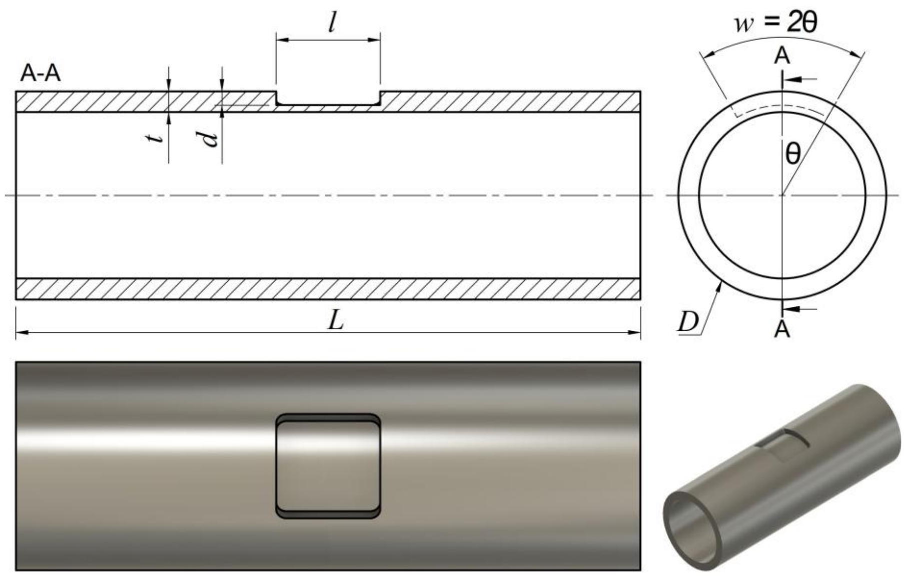

Figure 1. Geometry of the rectangular corrosion defect used in the validation study.

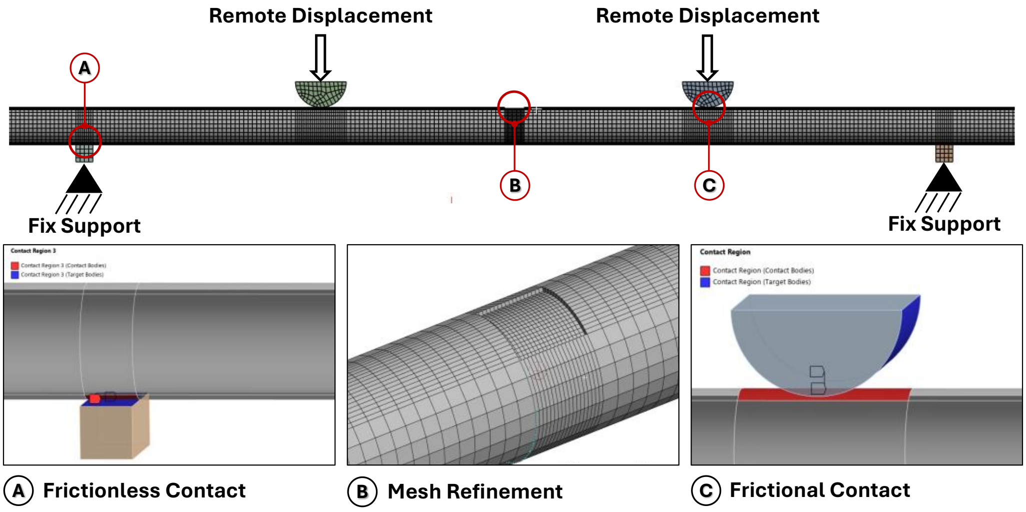

Figure 2. Boundary conditions of the full validation model.

The numerical responses were compared with the experimental data reported by Yu, Vargas and Karr (2012), as shown in Fig. 3. The predicted moment–rotation curves reproduce the overall response under both pure bending and combined bending–pressure loading, with discrepancies of less than 10%. The remaining differences are attributable to variations in material inputs, modeling idealizations, and contact representations. The validation also considered the deformation mechanism rather than the peak moment alone. Fig. 4 shows localized ovalization and compressive wrinkling in the corroded region, consistent with the experimentally reported deformation morphology. The benchmark therefore supports the FE procedure's ability to reproduce the global bending response and defect-induced local deformation of corroded pipes.

The available benchmark experiment used a rectangular corrosion defect, whereas the parametric study considers a semi-elliptical defect. The validation should therefore be interpreted as a framework-level benchmark for nonlinear bending response, pressure–bending interaction, and defect-induced local deformation, rather than as direct experimental validation of the semi-elliptical morphology.

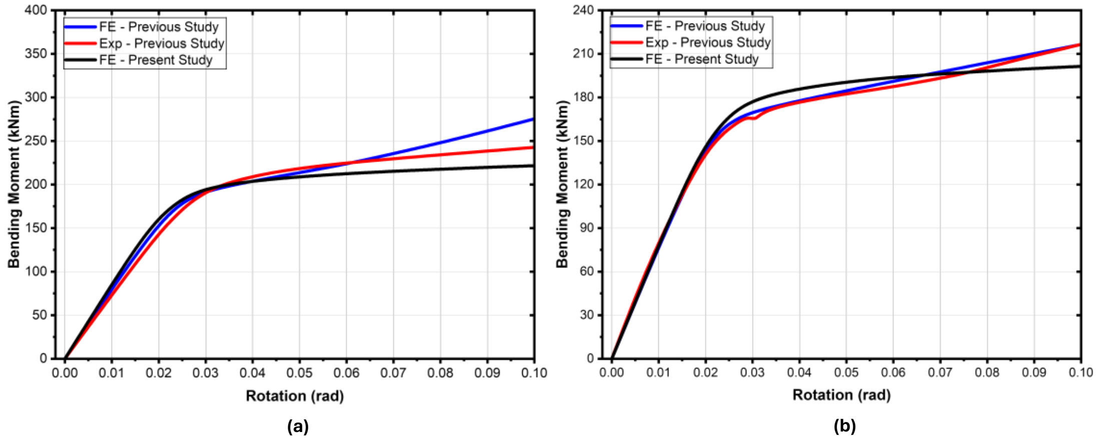

Figure 3. Comparison between the present FE model and the four-point-bending test data on corroded pipes reported by Yu, Vargas and Karr (2012) for: (a) pure bending; and (b) combined bending and internal pressure.

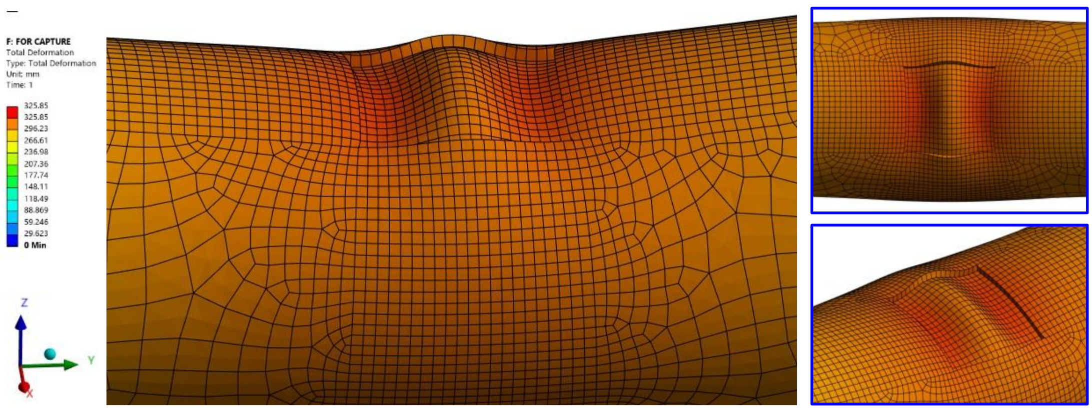

Figure 4. Deformation mode under pure bending, showing localized ovalization and wrinkling at the defect region (for comparison, see Yu, Vargas and Karr (2012)).

3.2. Material Properties

The pipe material considered in this study was API 5L X52 steel and was modeled as an isotropic elastoplastic material. The elastic properties consisted of a Young’s modulus of 200 GPa and a Poisson’s ratio of 0.3. The nominal yield strength was 390 MPa, while the engineering ultimate tensile strength was 520 MPa.

The nonlinear material response was represented using a multilinear isotropic hardening model. The true stress–plastic strain curve adopted as the FE material input is shown in Fig. 5 and was obtained from the published API 5L X52 material data. According to the adopted material data, the true ultimate stress was 612 MPa at a true strain of 0.1745. The material curve continued beyond this point and reached a terminal true-stress value of approximately 690 MPa at specimen fracture. Therefore, the value of 612 MPa represents the reported true ultimate stress, whereas the terminal value of approximately 690 MPa represents the final stress point included in the FE material-input curve. Consequently, local von Mises stresses approaching the terminal flow-stress level of the adopted curve may occur in highly deformed regions near the corrosion defect.

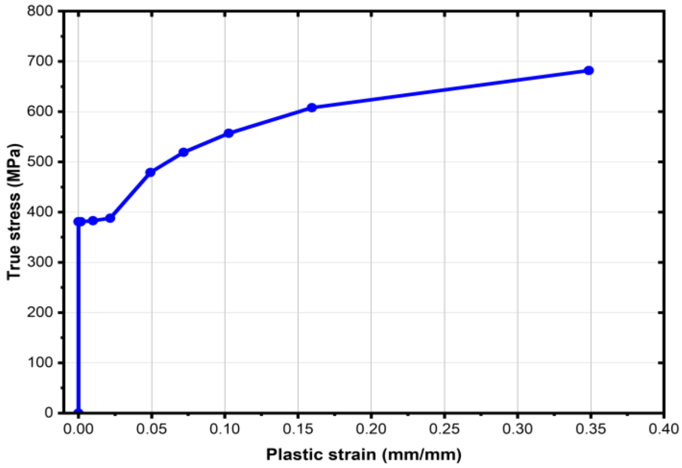

Figure 5. Literature-derived true stress–plastic strain input curve for API 5L X52 steel, adapted from Arumugam, Karuppanan and Ovinis (2020).

A multilinear isotropic hardening model was selected because the present analysis involves progressive plastic deformation before collapse. An elastic-perfectly plastic material model would not adequately represent strain hardening after yielding and could misrepresent the moment–rotation response in the post-yield regime. Isotropic hardening was considered appropriate because the simulated loading path involved monotonic bending under constant internal pressure; therefore, cyclic plasticity and the Bauschinger effect were not expected to be dominant mechanisms.

3.3. Model Geometry and Defect Parameter

The corrosion defect was idealized as a semi-elliptical wall-thinning region, as shown in Fig. 6. The defect geometry is defined by the maximum corrosion depth (d), axial length (l), and circumferential width (w). In the present study, the defect width was kept proportional to the corrosion depth using ($w = 2d$), while (d/t) and (l/D) were varied parametrically. This definition ensures that the deepest point of the defect is located at the center of the metal-loss region and that the wall thickness gradually increases toward the intact pipe surface. The remaining wall thickness at the deepest point is therefore $t_d = t - d$. This idealized morphology represents a controlled, semi-elliptical metal-loss profile rather than an irregular field-corrosion pattern.

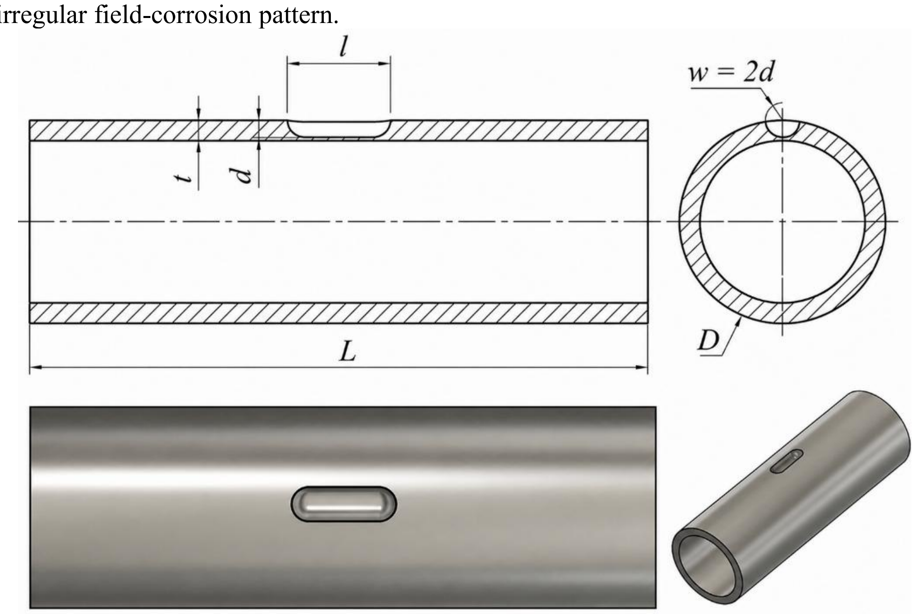

Figure 6. Corrosion defect for the present study

The investigated parameters are summarized in Table 1. The corrosion depth ratio was varied from 0.1 to 0.8, the axial defect length ratio from 0.2 to 1.2, and the internal pressure from 0 to 20 MPa. A selected simulation matrix of 33 finite-element cases was used instead of a full-factorial combination to examine the individual trends associated with corrosion depth, defect length, and internal pressure, while maintaining a practical computational cost for nonlinear large-deformation analysis. The selected depth range covers conditions from shallow wall thinning to severe metal loss, whereas the selected length range represents short, intermediate, and relatively long axial defects. For the investigated pipe, the reference pressure is approximately 60.7 MPa; therefore, the maximum applied pressure corresponds to a normalized pressure of approximately 0.32. This range was selected to evaluate pressure–bending interaction without shifting the dominant failure response towards pure burst failure.

Table 1. Defect parameters and loading scenario

No	Parameter	Value
1	Overall pipe length (L) in mm	1500
2	Outer diameter (D) in mm	300
3	Nominal wall thickness (t) in mm	20
4	Corrosion depth ratio (d/t)	0.1, 0.2, 0.3, 0.4, 0.5, 0.6, 0.7, and 0.8
5	Corrosion axial length ratio (l/D)	0.2, 0.4, 0.6, 0.8, 1.0, and 1.2.
6	Corrosion width (w)	$w = 2d$
7	Internal Pressure (MPa)	0.0, 2.5, 5.0, 7.5, 10.0, 12.5, 15.0, 17.5, and 20.0

3.4. Boundary Condition and Meshing Strategy

Full-scale four-point bending models with contact interfaces were used for the validation study. However, under large rotation and ovalization, moving contact surfaces increased computational cost and could cause convergence difficulties in the parametric simulations (Prabowo *et al.*, 2023, 2024; Suryanto *et al.*, 2026). Therefore, the parametric study used a symmetric quarter model with displacement-controlled loading. The quarter model was based on the symmetry of the pipe geometry, the defect position, the loading configuration, and the support conditions. Symmetry boundary conditions were applied on the longitudinal and transverse planes to retain the bending-dominated deformation and local ovalization at the defect region.

The nonlinear finite element analyses were performed using an implicit static structural solution procedure in ANSYS Mechanical. Geometric nonlinearity was accounted for by activating the large-deflection formulation, as the pipe exhibited cross-sectional ovalization, local wall distortion, and large plastic deformation prior to collapse. The pressure load was applied only to the cylindrical inner surface. No end-cap pressure, fluid domain, or equivalent axial pressure thrust was imposed. Accordingly, the model does not directly prescribe the conventional closed-ended longitudinal pressure stress. Bending deformation was then imposed incrementally to improve numerical stability during nonlinear plastic deformation and local buckling. The solution was carried out using one load step with a step end time of 1 s. Automatic time-stepping was enabled and defined using substeps, with 20 initial, 20 minimum, and 200 maximum substeps. A direct solver was used for the nonlinear equilibrium solution. Weak springs and inertia relief were deactivated. The convergence assessment was controlled by the default program-controlled convergence criteria in ANSYS Mechanical. When severe local deformation occurred near the corrosion defect, the automatic time-stepping procedure allowed smaller load increments within the prescribed substep range. The ultimate bending moment was defined as the maximum converged moment obtained from the moment–rotation response.

Prior to the parametric analysis, a mesh convergence study was conducted to ensure that the numerical predictions were independent of the discretization (Cao *et al.*, 2016; Prabowo *et al.*, 2022; Faizatama *et al.*, 2025; Samaei and Ghahfarokhi, 2025; Riffat, Samaei and Ghahfarokhi, 2025). The assessment was conducted using a severe-defect configuration with d/t = 0.8, l/D = 1.0, and an internal pressure of 10 MPa. This configuration was selected because it produces pronounced localized plastic deformation and is therefore the most sensitive to mesh density. The boundary conditions were set according to the symmetric quarter-four-point bending configuration shown in Fig. 7, and the meshing strategy is illustrated in Fig. 8.

The model was primarily discretized with mapped hexahedral elements using SOLID186 quadratic solid elements. In geometrically constrained regions where mapped meshing was infeasible, SOLID187 tetrahedral elements were locally used to maintain mesh continuity. The mesh density was characterized by the number of elements through the nominal pipe wall thickness at the defect region (n) (Nourpanah and Taheri, 2012; Khodaei *et al.*, 2026). Several meshes with different element sizes were generated, resulting in n-values ranging from 1 to 10. For each mesh, the ultimate bending moment was extracted from the moment-rotation response and normalized by the value obtained from the finest mesh. Element quality was monitored during mesh generation. Mesh quality in the critical regions, particularly around the corrosion defect, was controlled by maintaining a Jacobian ratio greater than 0.9. The selected mesh density used four elements through the nominal pipe wall thickness at the defect region, as justified by the mesh convergence study. Since the same meshing strategy was applied consistently across all parametric cases, the observed differences in ultimate bending capacity are attributed primarily to changes in corrosion geometry and internal pressure rather than to numerical discretization effects. Fig. 9 shows that the predicted ultimate moment approaches asymptotic stability as the mesh is refined. The mesh with $n = 4$ was selected for the parametric simulations because further refinement produced only minor changes in the global capacity and the observed stress concentration and local deformation patterns around the defect.

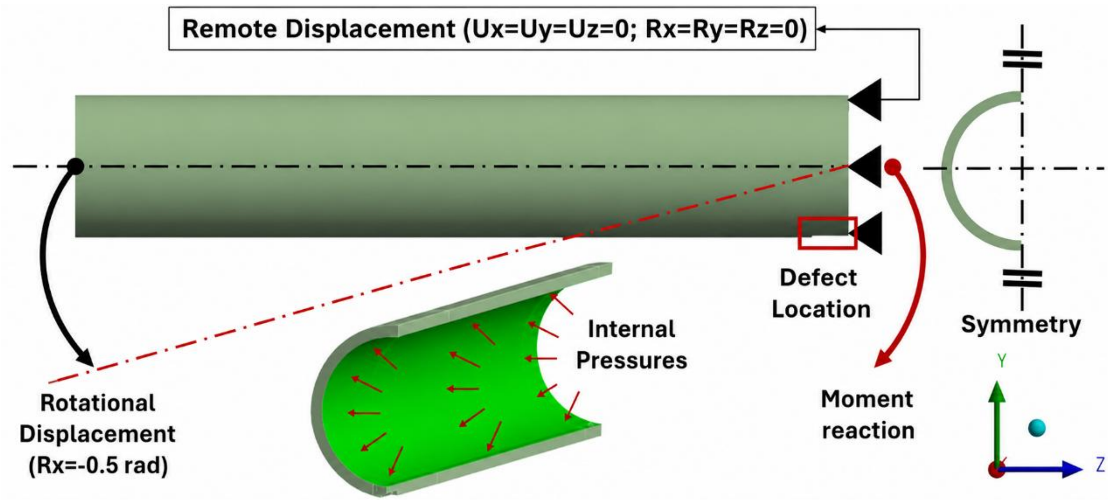

Figure 7. Boundary condition of the quarter model

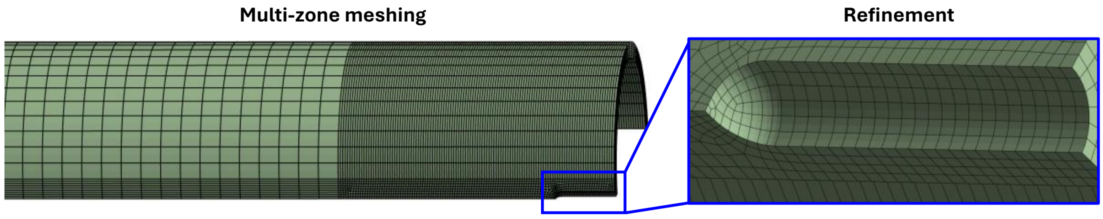

Figure 8. Meshing strategy

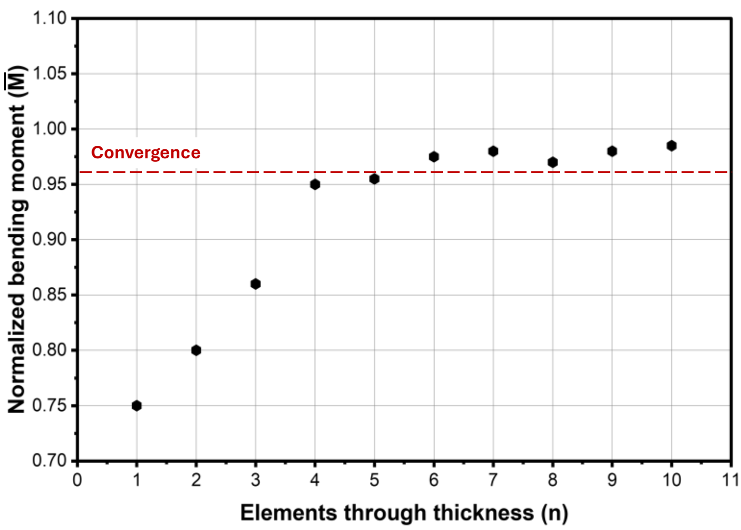

Figure 9. Mesh convergence based on the number of elements through the nominal pipe wall thickness.

3.5. Modeling Uncertainty and Study Limitation

This study uses deterministic nonlinear finite element simulations. Mesh sensitivity was evaluated by varying the number of elements through the pipe wall thickness. The selected mesh was adopted after the normalized ultimate bending moment changed by less than approximately 1% with further refinement. However, the study does not include a formal probabilistic uncertainty quantification or global sensitivity analysis.

The predicted response may be affected by material properties, boundary conditions, defect geometry, and initial geometric imperfections. The material properties were treated as fixed values, and variations in yield strength, ultimate tensile strength, and strain-hardening behavior were not considered. The quarter-symmetry model also assumes ideal geometry, symmetric loading, and a centrally located defect. Actual subsea pipelines may contain irregular or multiple defects and may experience non-symmetric bending.

The semi-elliptical defect represents an idealized local wall-thinning profile. Actual corrosion may have irregular shape, non-uniform depth, rough surfaces, or interacting pits, which may affect stress concentration and local buckling. In addition, residual stress, welding effects, initial imperfections, and variable operational loads were not included. The benchmark experiment used rectangular corrosion defects. Therefore, the validation supports the FE framework and the main bending-collapse mechanisms, but it does not directly validate the semi-elliptical defect geometry. The reported results should be interpreted as deterministic comparative estimates for the investigated conditions, rather than as design resistance values. Future work should include experimental tests on semi-elliptical defects and reliability-based assessment of modeling and loading uncertainties.

4. Results and Discussion

The numerical results are presented in normalized form to compare the effects of corrosion geometry and internal pressure. The bending moment and pressure are normalized using Eqs. (4)–(6). For the investigated pipe, the reference bending moment used for normalization is approximately 715 kNm, and the reference pressure is approximately 60.7 MPa. The following discussion links the FE results to three main mechanisms: wall-thickness reduction, pressure-induced membrane stress, and local shell instability.

4.1. Stress Distribution and Local Collapse Mechanism

Fig. 10 compares the von Mises stress distributions of the intact and corroded pipes under bending-dominated deformation. The intact pipe exhibits a relatively smooth, broadly distributed stress field along its wall. This response indicates that the applied bending moment is resisted by the full pipe cross-section, with stress redistributed over a comparatively wide circumferential and longitudinal region. Such behavior is consistent with the bending-stress interpretation introduced in Eqs. (7) and (8), in which the longitudinal bending stress is governed primarily by the global section properties of the intact pipe. For the intact configuration, the maximum displayed von Mises stress is 520.73 MPa. However, the stress contour does not show severe localization at a single critical point. Instead, the stress field remains broadly distributed over the pipe wall, indicating that the intact section retains the ability to mobilize a relatively stable bending response before local collapse develops.

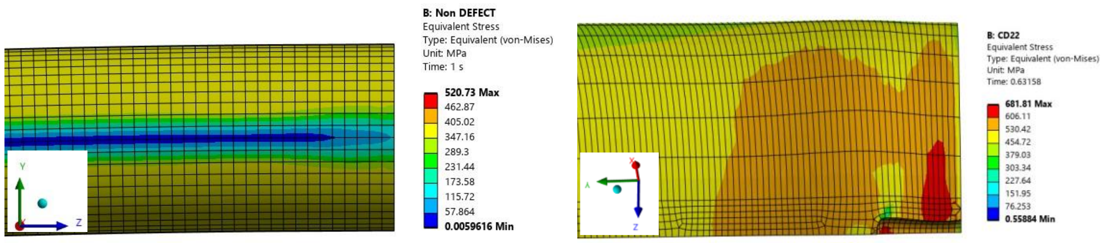

(a) (b)

Figure 10. Von Mises stress distribution at 0.2 rad rotational displacement of: (a) the intact pipe; and (b) the corroded pipe. The intact pipe shows a distributed stress field, whereas the corroded pipe exhibits stress concentration around the defect shoulder and remaining ligament.

A markedly different response is observed in the corroded pipe. The stress field is strongly localized around the defect shoulder and the remaining ligament. The maximum von Mises stress reaches 681.81 MPa. This value is approximately 30.9% higher than that of the intact pipe. It is also close to the terminal true-stress level of approximately 690 MPa in the adopted multilinear isotropic hardening material-input curve. The increase in stress is caused by the reduced wall thickness and the altered local stress-transfer path around the semi-elliptical defect. The stress contour is used mainly to identify the location and relative severity of stress concentration. The ultimate bending capacity is determined from the peak of the global moment–rotation response, rather than from the maximum stress contour alone.

Fig. 11 further shows that the corroded pipe reaches its ultimate capacity through localized wall distortion and buckling near the defect region. The deformation pattern indicates that the pipe wall loses local stability before a fully distributed plastic mechanism can develop across the entire cross-section. This observation is consistent with the local shell-stability framework described in Eqs. (17) and (18). As the residual wall thickness decreases, both the local shell bending rigidity and the local critical compressive resistance decrease. The remaining ligament therefore becomes more susceptible to ovalization, wrinkling, and local buckling. Localized yielding precedes local buckling in the defect region. In this study, the ultimate bending capacity is determined from the peak moment, together with the onset of visible local wall distortion. The quantitative effects of corrosion depth, defect length, and internal pressure are examined in the following sections.

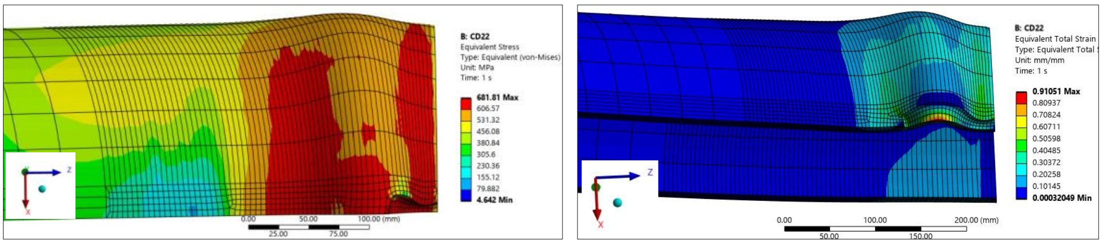

(a) (b)

Figure 11. Local buckling mode of the corroded pipe at the ultimate bending capacity: (a) von Mises stress distribution; and (b) total strain contour

4.2. Moment–Rotation Response

Fig. 12 presents the moment-rotation response for the intact pipe, the corroded pipe, and the corroded pipe subjected to internal pressure. The bending moment shown in this response is obtained from the FE reaction at each rotation level. In the initial stage, the response increases almost linearly, indicating that the deformation is dominated by elastic flexural stiffness. This trend is consistent with the curvature–moment relation introduced in Eq. (22) and the rotation–curvature interpretation in Eq. (23).

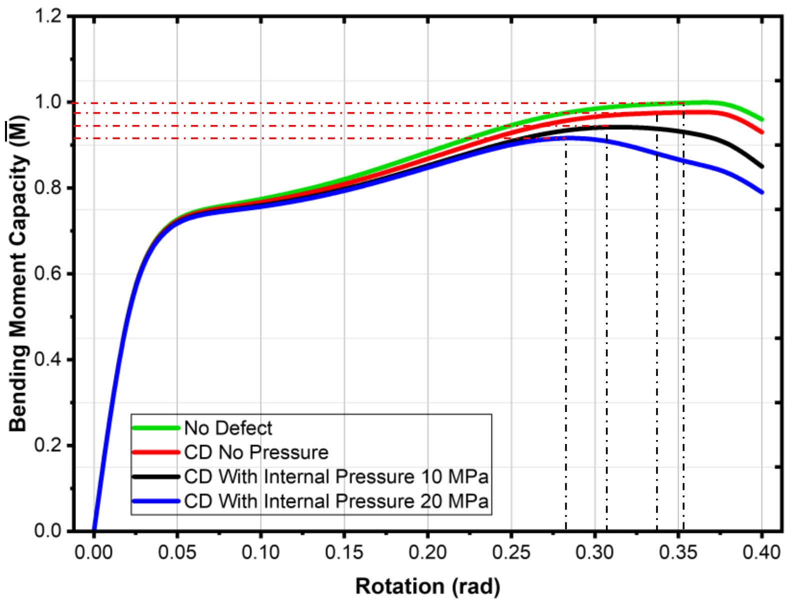

Figure 12. Moment–rotation responses of the intact pipe, corroded pipe, and pressurized corroded pipe. Corrosion reduces the ultimate bending moment by promoting local stress concentration, while internal pressure further decreases the bending capacity by accelerating yielding and local buckling at the defect region.

As rotation increases, the response becomes nonlinear because of material yielding, cross-sectional ovalization, and local wall deformation. The intact pipe shows the highest bending resistance and the most stable post-yield response because its full wall thickness and section modulus remain available. It can therefore mobilize broader plastic redistribution before reaching the peak moment. The corroded pipe reaches a lower ultimate bending moment. Wall thinning reduces the local section modulus and increases the local bending stress at the remaining ligament, as described by Eqs. (9)–(12). As a result, nonlinear deformation begins earlier, and the nominal bending resistance cannot be fully mobilized.

The reduction becomes more pronounced when internal pressure is applied. Although internal pressure may suppress ovalization in some intact thin-walled pipes, the present results show that this possible stabilizing effect is outweighed by the increased pressure-induced circumferential stress and the resulting multiaxial stress interaction at the corroded ligament. The pressurized corroded configurations at 10 and 20 MPa reach their ultimate capacity at lower bending moments than the unpressurized corroded pipe. Reduced wall thickness increases the local pressure-induced circumferential stress, while bending generates axial stress at the same defect region. Their interaction increases the local multiaxial stress demand and reduces the remaining margin to yielding and local instability. Thus, the moment-rotation curves confirm that pressure and bending should be treated as coupled loading components for corroded pipelines.

The semi-elliptical defect does not introduce an abrupt thickness discontinuity at its boundary. Nevertheless, the FE results show that the remaining ligament remains the critical location for stress concentration, plastic localization, and local buckling. This confirms that gradual wall thinning can still produce localized defect-controlled collapse under combined pressure and bending.

4.3. Effect of Corrosion Depth on Bending Capacity

Fig. 13 presents the effect of corrosion depth ratio on the normalized ultimate bending capacity at a fixed defect length ratio of $l/D = 1$. The results show a monotonic reduction in capacity as (d/t) increases. Under the present defect definition, the circumferential width is proportional to the corrosion depth $(\mathrm{w} = 2d)$. Therefore, the observed trend represents the effect of increasing defect severity, primarily through a reduction in the remaining ligament thickness.

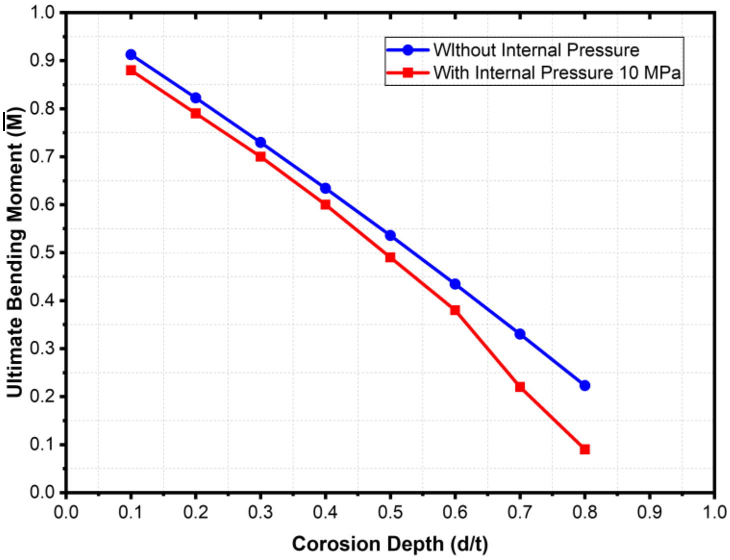

Figure 13. Effect of corrosion depth ratio on normalized ultimate bending capacity at $l/\mathrm{D} = 1$. Increasing defect severity reduces the residual wall thickness and promotes localized deformation at the defect region.

For shallow defects, the remaining ligament and surrounding intact wall retain sufficient stiffness to sustain a relatively high bending resistance. As the corrosion depth increases, deformation becomes increasingly concentrated at the defect region, and the peak bending moment decreases. This response is consistent with the reduced local load-carrying material, stronger stress concentration, and lower resistance to localized wall distortion described in Sections 2.4 and 2.6. Within the investigated parameter range, the corrosion depth ratio is therefore the principal defect-severity parameter governing the residual bending capacity.

4.4. Effect of Defect Axial Length on Bending Capacity

Fig. 14 presents the effect of defect axial length on the normalized ultimate bending capacity for a fixed corrosion depth ratio of $d/t = 0.5$. The normalized ultimate bending capacity decreases as the defect length ratio increases from $l/D = 0.2$ to $l/D = 1.2$. The reduction is more pronounced when the defect changes from a short to an intermediate axial length, whereas the capacity curve gradually approaches a plateau for longer defects.

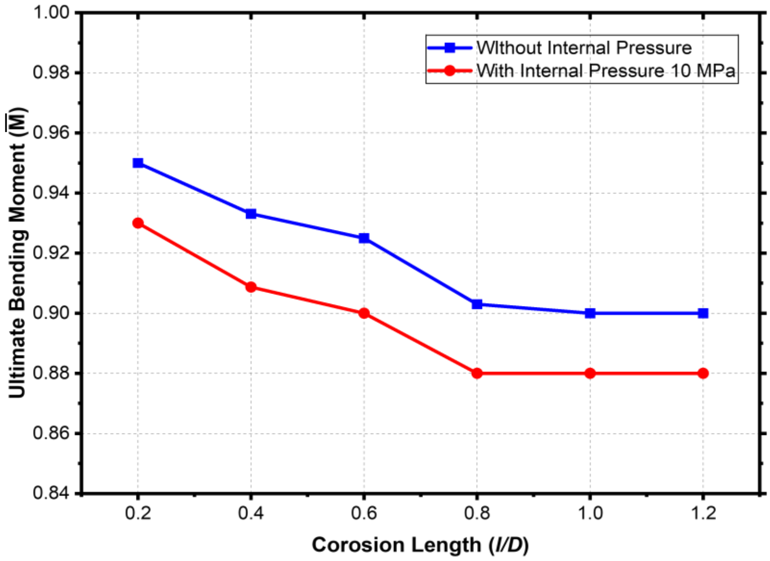

Figure 14. Effect of corrosion length ratio on normalized ultimate bending capacity at $d/t = 0.5$. The bending capacity decreases rapidly for short-to-intermediate defects, but the reduction becomes less significant for longer defects because collapse becomes governed by the weakest local ligament

This trend indicates that the axial extent of the weakened region influences the ability of the surrounding intact pipe wall to redistribute bending-induced deformation. For short and intermediate defects, increasing defect length reduces the contribution of the adjacent intact wall, resulting in a noticeable decrease in bending resistance. As the defect lengthens, the collapse response is governed primarily by the critical local ligament at the deepest point of the corrosion defect. Further extension of the defect along the pipe axis, therefore, produces only a limited additional reduction in ultimate capacity. Accordingly, defect axial length is most influential within the short-to-intermediate range considered in this study, whereas corrosion depth and local instability at the remaining ligament govern the response of sufficiently long defects.

4.5. Effect of Internal Pressure on Bending Capacity

Fig. 15 shows the influence of internal pressure on the normalized ultimate bending capacity for a pipe with $l/D = 1$ and $d/t = 0.5$. The normalized ultimate bending capacity decreases monotonically as internal pressure increases from 0 to 20 MPa. For this configuration, $\bar{M}_u$ decreases from approximately 0.95 at zero pressure to approximately 0.86 at 20 MPa, indicating that internal pressure acts as a detrimental loading component within the investigated pressure range.

The reduction in bending capacity is associated with the local stress state at the corroded ligament. In the present FE model, pressure is applied only to the cylindrical inner surface; therefore, its primary direct contribution is the pressure-induced circumferential stress. Because the wall thickness is reduced at the defect, this circumferential stress becomes more severe in the remaining ligament. Bending simultaneously generates longitudinal stress at the same location, and the combined stress state increases the local von Mises stress demand. Consequently, yielding and localized wall distortion develop at lower bending moments, thereby reducing peak capacity. Although internal pressure may suppress ovalization in some intact thin-walled pipes, the present results indicate that this potential stabilizing effect is outweighed by the stress concentration and reduced residual wall thickness at the semi-elliptical corrosion defect. Therefore, internal pressure and bending moment should be evaluated as coupled loading components when assessing the residual bending capacity of corroded pipelines.

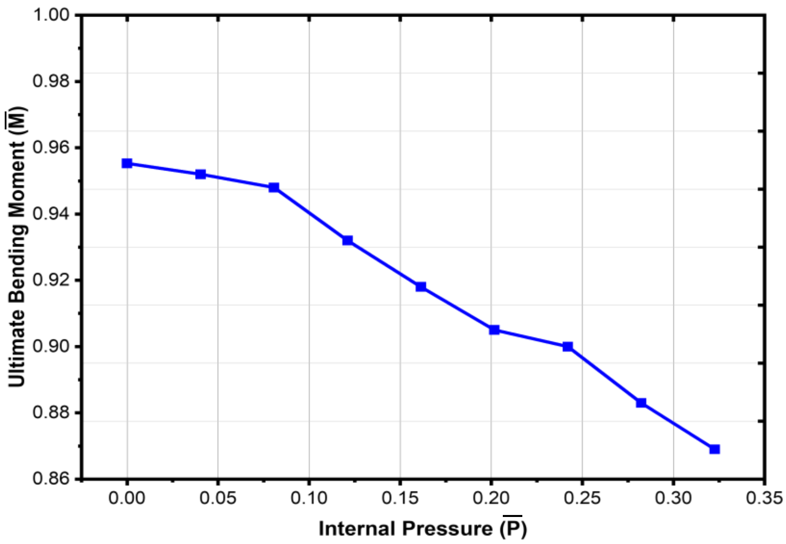

Figure 15. Effect of internal pressure on normalized ultimate capacity for $l/D = 1$ and $d/t = 0.5$.

5. Conclusions

This study evaluated the ultimate bending capacity of subsea CO_2 transport pipelines containing idealized semi-elliptical corrosion defects under combined internal pressure and bending moment using nonlinear finite element analysis. The results show that corrosion depth is the dominant geometric parameter controlling residual bending capacity. Increasing d/t reduces the remaining ligament thickness and promotes localized deformation at the defect region, resulting in a progressive reduction in normalized ultimate bending moment. The influence of axial defect length is most pronounced for short and intermediate defects. As the defect lengthens, the capacity reduction approaches a plateau because collapse is governed mainly by the critical local ligament rather than by the total axial extent of wall thinning. Within the investigated loading range, internal pressure reduces the ultimate bending capacity of the corroded pipe. The pressure-induced circumferential stress interacts with the bending-induced longitudinal stress at the defect ligament, increasing the local multiaxial stress demand and promoting earlier localized deformation. The results are limited to deterministic simulations of a single idealized semi-elliptical defect, the selected material model, and the investigated loading and boundary conditions. Further work should include experimental validation of semi-elliptical defects, imperfection-sensitivity analysis, and reliability-based assessment under representative subsea operating conditions.

Acknowledgements

This research was funded by the Indonesian Endowment Fund for Education (LPDP) under the auspices of the Indonesian Ministry of Higher Education, Science and Technology, and administered through the EQUITY Program of Universitas Sebelas Maret. The funding was provided under the "International Research Network Program EQUITY THE Impact Rankings 2025" scheme, with Contract No. 4315/B3/DT.03.08/2025 and No. 84/UN27/KS/2025, as stated in the signed document with ID No. 4141.1/UN27.22/PT.01.03/2025. The authors gratefully acknowledge this financial and institutional support.

References

Arumugam, T., Karuppanan, S. and Ovinis, M. (2020) "Finite element analyses of corroded pipeline with single defect subjected to internal pressure and axial compressive stress," *Marine Structures*, 72, 102746. https://doi.org/10.1016/ j.marstruc.2020.102746.

Bhardwaj, U., Teixeira, A.P. and Soares, C.G. (2020) "Reliability assessment of a subsea pipe-in-pipe system for major failure modes," *International Journal of Pressure Vessels and Piping*, 188, 104177. https://doi.org/10.1016/j.ijpvp.2020. 104177.

Cao, B. *et al.* (2016) "Numerical Analysis for Damage Characteristics Caused by Ice Collision on Side Structure," in *Proceedings of the ASME 2016 35th International Conference on Ocean, Offshore and Arctic Engineering. Volume 8: Polar and Arctic Sciences and Technology; Petroleum Technology*. Busan: American Society of Mechanical Engineers, V008T07A019. https://doi.org/10.1115/OMAE2016-54727.

Chen, Z.-F. *et al.* (2024) "Study on burst pressure of subsea pipelines with asymmetrical corrosion defects," *Engineering Failure Analysis*, 155, 107722. https://doi.org/10.1016/j.engfailanal.2023.107722.

Conde, J. *et al.* (2023) "Design of pin connections between steel members," *Journal of Constructional Steel Research*, 201, 107752. https://doi.org/10.1016/j.jcsr.2022.107752.

Elchalakani, M., Zhao, X.L. and Grzebieta, R.H. (2002) "Plastic mechanism analysis of circular tubes under pure bending," *International Journal of Mechanical Sciences*, 44(6), 1117–1143. https://doi.org/10.1016/ S0020-7403(02)00017-6.
Faizatama, A.M. *et al.* (2025) "Hydrodynamic impact of cold-water pipes and mooring systems on KVLCC2 for floating OTEC platforms," *Ocean Engineering*, 341, 122491. https://doi.org/10.1016/j.oceaneng.2025. 122491.
Gao, B. *et al.* (2024) "Finite element analysis of the limit load of pipe bend with local wall-thinning defect under complex loads," *International Journal of Pressure Vessels and Piping*, 208, 105141. https://doi.org/ 10.1016/j.ijpvp.2024. 105141.
Khodaei, M. *et al.* (2026) "Numerical and experimental investigation of liner wrinkling and strain localisation in mechanically lined pipes under bending," *Applied Ocean Research*, 166, 104859. https://doi.org/10.1016/ j.apor.2025.104859.
Korol, R.M. and Hudoba, J. (1972) "Plastic Behavior of Hollow Structural Sections," *Journal of the Structural Division*, 98(5), 1007–1023. https://doi.org/10.1061/JSDEAG.0003221.
Lo, M., Karuppanan, S. and Ovinis, M. (2022) "ANN- and FEA-Based Assessment Equation for a Corroded Pipeline with a Single Corrosion Defect," *Journal of Marine Science and Engineering*, 10(4), 476. https://doi.org/10.3390/jmse 10040476.
Ma, Y. *et al.* (2025) "The longitudinal mechanical behavior of steel pipes with pitting corrosion under the coupling effect of complex service loads," *International Journal of Pressure Vessels and Piping*, 214, 105423. https://doi.org/10.1016/ j.ijpvp.2024.105423.
Nourpanah, N. and Taheri, F. (2012) "A Comprehensive Parametric Finite Element Study on the Development of Strain Concentration in Concrete Coated Offshore Pipelines," *Journal of Pressure Vessel Technology*, 134(6), 061701. https://doi.org/10.1115/1.4006556.
Prabowo, A.R. *et al.* (2022) "Forecasting the Effects of Failure Criteria in Assessing Ship Structural Damage Modes," *Civil Engineering Journal*, 8(10), 2053–2068. https://doi.org/10.28991/CEJ-2022-08-10-03.
Prabowo, A.R. *et al.* (2023) "Comparative study of shell element formulations as NLFE parameters to forecast structural crashworthiness," *Curved and Layered Structures*, 10(1), 20220217. https://doi.org/10.1515/ cls-2022-0217.
Prabowo, A.R. *et al.* (2024) "Crushing resistance on the metal-based plate under impact loading: A systematic study on the indenter radius influence in grounding accident," *Applications in Engineering Science*, 18, 100177. https://doi.org/ 10.1016/j.apples.2024.100177.
Riffat, J., Doudran, H.A. and Samaei, S.R. (2025) "AI-driven digital twin for uncertainty-aware structural health monitoring of offshore wind turbines considering biofouling effects and reliability prediction," *Green Technology & Innovation*, 1(2), 025330013. https://doi.org/10.36922/GTI025330013.
Riffat, J., Nazari, K. and Samaei, S.R. (2026) "AI-Driven Digital Twin Framework for Adaptive and Real-Time Structural Health Monitoring of Offshore Marine Structures," *Artificial Intelligence for Sustainable Cities*, 1(1), 90–104. https://doi.org/10.65582/aifsc.2026.006.
Riffat, J., Samaei, S.R. and Ghahfarokhi, M.A. (2025) "AI-Based Optimization and Hydrodynamic Performance of Floating Pontoon Breakwaters through Experimental and Numerical Modeling," *Global Decarbonisation*, 1(1), 1–26. https://doi.org/10.17184/eac.9847.
Samaei, S.R. and Ghahfarokhi, M.A. (2025) "Hydrodynamic Assessment of Floating Dock Behavior: A Case Study in Bahonar Port, Bandar Abbas," *Energy Catalyst*, 1(1), 104. https://doi.org/10.61552/EC.2025.008.
Shuai, Y. *et al.* (2022) "A novel model for prediction of burst capacity of corroded pipelines subjected to combined loads of bending moment and axial compression," *International Journal of Pressure Vessels and Piping*, 196, 104621. https://doi.org/10.1016/j.ijpvp.2022.104621.
Sinclair, G.B. and Helms, J.E. (2015) "A review of simple formulae for elastic hoop stresses in cylindrical and spherical pressure vessels: What can be used when," *International Journal of Pressure Vessels and Piping*, 128, 1–7. https://doi.org/10.1016/j.ijpvp.2015.01.006.
Suryanto, S. *et al.* (2026) "Structural integrity of designed sandwich panels under low temperature conditions: blast effect assessment using finite element simulation," *Journal of the Brazilian Society of Mechanical Sciences and Engineering*, 48(1), 28. https://doi.org/10.1007/s40430-025-06013-x.
Udonsek, D.E., Tamonodukobipi, D. and Odokwo, V.E. (2023) "Corrosion-Based Integrity Analysis of Offshore Pipeline for Hydrocarbon Transportation," *Journal of Power and Energy Engineering*, 11(5), 24–41. https://doi.org/10.4236/ jpee.2023.115002.
Yu, W., Vargas, P.M. and Karr, D.G. (2012) "Bending Capacity Analyses of Corroded Pipeline," *Journal of Offshore Mechanics and Arctic Engineering*, 134(2), 021701. https://doi.org/10.1115/1.4004521.
Zhang, D. *et al.* (2025) "Experimental study of the full-scale burst failure behavior of carbon dioxide steel pipeline," *Journal of Pipeline Science and Engineering*, 5, 100221. https://doi.org/10.1016/j.jpse.2024.100221.
Zhou, L. *et al.* (2025) "Evaluation on collapse behaviour of thick-walled pipes with corrosion defect under combined external pressure, axial tension and bending moment," *Structures*, 75, 108593. https://doi.org/10.1016/ j.istruc.2025.108593.
Zhou, L. *et al.* (2026) "Theoretical and numerical studies on collapse of corroded subsea pipelines under combined external pressure and axial tension," *Marine Structures*, 106, 103964. https://doi.org/10.1016/j.marstruc. 2025.103964.
Zhu, X.-K. and Leis, B.N. (2012) "Evaluation of burst pressure prediction models for line pipes," *International Journal of Pressure Vessels and Piping*, 89, 85–97. https://doi.org/10.1016/j.ijpvp.2011.09.007.